Performance analysis and optimal sizing of electric multirotors

Published Version:
de Angelis E.L., Giulietti F., Rossetti G., Bellani G. (2021). Performance analysis and optimal sizing of electric multirotors. AEROSPACE SCIENCE AND TECHNOLOGY, 118, 1-15 [10.1016/j.ast.2021.107057].

Availability:
This version is available at: https://hdl.handle.net/11585/844724 since: 2024-08-30

Published:
DOI: http://doi.org/10.1016/j.ast.2021.107057

Performance Analysis and Optimal Sizing of Electric Multirotors

Emanuele L. de Angelis[*,1], Fabrizio Giulietti[2], Gianluca Rossetti[3], Gabriele Bellani[4]

University of Bologna, Forlí, Italy 47121

Abstract

This paper presents an analytical framework for addressing the hovering performance of a battery–powered multirotor. The estimation of power required for flight is investigated and an analytical model is proposed to describe the rotor figure of merit as a function of few relevant blade parameters, without the need for ad hoc experiments. The model is derived after a discussion about the aerodynamics of rotating blades. The formulation in terms of Reynolds number is supported by an experimental campaign, performed on a set of commercial–of–the–shelf propellers optimized for small–scale multirotor applications.

By imposing the balance between required and available power, the hovering time is predicted by an integral formulation developed for a constant–power battery discharge process. The best endurance condition is obtained in terms of optimum battery capacity and flight time. The methodology, applicable to the design phase of novel multirotor configurations, is finally validated by flight tests.

[*]Corresponding author

[1]Research Fellow, Department of Industrial Engineering (DIN), emanuele.deangelis4@unibo.it

[2]Associate Professor, Department of Industrial Engineering (DIN), fabrizio.giulietti@unibo.it

[3]Research Fellow, Interdepartmental Center for Industrial Research (CIRI Aerospace), gianluca.rossetti3@unibo.it

[4]Assistant Professor, Department of Industrial Engineering (DIN), gabriele.bellani2@unibo.it

1. Introduction

Remotely–Piloted Aerial Systems (RPAS), particularly small battery–powered fixed and rotary–wing platforms, gained a large interest in the scientific community. Reduced size, weight, and operational costs, in fact, make such systems one of the most suitable solutions for a wide range of applications, including load transportation, search and rescue, risk management, surveillance, aero–photogrammetry, and, in general, remote sensing activities [1, 2].

Among the available rotary–wing configurations, multirotors proved to be particularly attractive [3]. On the one hand, low structural complexity and simplicity of use allow for operative cost reduction. On the other hand, the hovering and vertical take–off and landing capabilities empower effective operations in restricted and obstructed areas [4, 5]. Also, with respect to a conventional helicopter with the same take–off weight, a multirotor is typically characterized by a more compact size, with satisfactory robustness to external disturbances and improved maneuvering capabilities [6, 7]. Such features are achieved by spreading the total disc area into multiple propulsion units, where the use of smaller propellers rotating at a higher speed comes at the cost of a loss in efficiency with respect to the conventional, single–rotor configuration. This, in addition to the limited endurance–to–weight ratio typical of electrically–driven systems, makes the performance of the hovering condition a critical, but challenging, issue. In this respect, the larger demand for high endurance RPAS operations, has increased the interest on research programs which aim at deriving numerical and analytical tools for range/endurance prediction and optimal preliminary sizing [8].

Most of the available multirotor configurations use MH–Ni, Li–Po, and Li–Ion battery packs. Due to their long life, small self–discharge, and high energy–to–weight ratio, Li–Po and Li–Ion systems have become the most widespread solution to power supply, provided a suitable Battery Management System (BMS) is designed to ensure safety and efficiency of battery usage [9]. The basic functions of a BMS include battery data acquisition, modeling and state estimation, charge and discharge control, fault diagnosis and alarm, thermal management, balance control, and communication. Battery modeling and state estimation are thus key functions of advanced BMS, allowing for reliable operation of unmanned systems, optimize the battery configuration, and provide a basis for safety management [10]. The battery models presented in literature mainly fall into the following three categories: a) physics–based electrochemical models [11], b) electrical equivalent circuit models [12], and c) data–driven models established by artificial intelligence algorithms such as neural networks or support vector machines [13]. With respect to the battery state estimation problem, different techniques have been proposed in order to characterize the state–of–charge/state–of–energy. These methods include a) the use of look–up tables, b) -hour integral routines, c) recursive algorithms based on Kalman–like [14] or particle filter approaches, d) state–observers, e) data–driven based methods, such as neural networks, fuzzy–logic and genetic algorithms, support vector machines [15].

Early studies investigating the performance and sizing of battery–powered aircraft became available only at the beginning of the last decade, based on Peukert's modeling of the discharge process [16]. In particular, numerical and analytical solutions addressing electric aircraft performance are presented in [17], where the effects of absorbed current on residual battery capacity are considered. In Ref. [18] the best range condition is discussed in detail while in [19] endurance estimates are validated by means of an experimental campaign. With regard to multirotor vehicles, a closed–form solution for endurance analysis as well as an optimal sizing approach for the battery pack is provided in [20], where the configuration for maximum endurance is outlined in terms of rotorcraft design features and optimal battery capacity, after a test–bed characterization of the powerplant. Lindahl et al. [21] propose a sizing tool to select a good combination of propulsion components, based on a linear approximation to the ohmic region of the battery discharge law. Using momentum theory and blade element theory, Latorre [22] offers an optimal design for the electric power system of a quadrotor using the identification method, and proposes a mathematical model to select the optimal motor. Kaya et al. [23] use a polynomial model to estimate the motor–propeller pair performance (from the endurance point of view), based on collected test data and under the assumption of constant current discharge. By introducing the notions of available capacity and usable capacity factors, Abdilla et al. [24] obtain an endurance formula model for rotorcraft driven by Li–Po batteries. The same authors finally propose a technique to optimize the endurance of rotorcraft by sub–dividing the monolithic battery into multiple smaller–capacity batteries, which are then sequentially discharged and released [25].

The above mentioned approaches, typically based on Peukert's equation, stem from the simplifying assumption of a constant–current discharge model. However, it must be noted that a constant–power battery discharge process is more representative of fixed–wing steady–level flight or hovering of battery–

powered rotorcraft. To this aim, Fuller [26] developed a battery discharge model, based on a modification of Peukert's law, to predict the terminal voltage and current for a constant–power process. Finally, a novel constant–power integral formulation of battery discharge process was derived, based on experimental data, in Ref. [27] by some of the present authors. This model provides a complete framework for performance analysis and optimal preliminary sizing of fixed–wing platforms.

In order to fully predict and optimize the performance of electric rotorcraft, however, battery modeling is only the starting point. The complete propulsion system needs to be characterized, with particular attention to the generation of thrust from selected propellers. In Ref. [28] the aerodynamic efficiency of small–scale propellers is addressed also under non–axial inflow conditions, whereas in [29] a mathematical model of the engine thrust/RPM function for low Reynolds number applications is presented. With respect to multirotor sizing, recent works address the problem by means of scaling laws and similarity models [30], and by using a hybrid approach which integrates theoretical formulations, computational fluid dynamics, and experimental validation [31, 32, 33]. Other approaches to the throttle/thrust and thrust/power functions description are obtained by experimental validations [34, 35], manufacturer data [36], or CFD analysis [37].

In what follows, the total power required for the hovering condition is calculated according to the procedure presented in [38]. Then, in order to characterize the aerodynamic behavior of the propeller, an analytical model is proposed to describe the rotor figure of merit as a function of few relevant blade parameters. To this aim, results of the classical Blade Element (Momentum) Theory (BET) [39] are enhanced by introducing an empirical correction function allowing for a more accurate prediction of the required blade tip speed, for a given thrust condition. Following a similar approach, a semi–empirical expression of the figure of merit as a function of blade Reynolds number [40] and propeller pitch/diameter ratio is finally derived. These results are obtained thanks to a dedicated experimental campaign performed on a selection of commercial–of–the–shelf propellers, optimized for small–scale multirotor applications. At the cost of few simplifying assumptions, flight endurance is analytically evaluated according to the battery model presented in [27], adapted for the first time to the analysis of multirotor platforms.

Finally, such model is applied to prove the existence of an optimal battery configuration (namely the configuration determining the maximum hovering endurance). In fact, unlike conventional fuel–powered vehicles, where an increased fuel fraction always provides increased endurance and range, the weight of electrically–powered vehicles remains constant. Hence, the beneficial effect of weight loss during flight is not experienced [20]. In this case, increasing battery weight may not necessarily provide an increased endurance and/or range, if the energy cost of lifting more weight overcomes the benefit of the increased battery–pack capacity. Generally speaking, the solution to the optimal sizing of battery packs is a challenging issue, which involves different kinds of electric vehicles. Wang et al. [41] prove that the range- and energy–optimal design points can be considered concurrently in design optimization of small electric aircraft: for a given flight task and performance objective, the approach incorporating the dynamic battery model and static component model provides an optimal flight trajectory and the corresponding battery package parameters. In [42] convex modeling steps are introduced to simultaneously optimize battery sizing and energy management of hybrid electric vehicle powertrains. An investigation is also provided where results from convex optimization are compared to those obtained with dynamic programming. In [43] the joint optimization problem of battery mass and flight trajectory for high–altitude solar–powered aircraft is discussed. In particular, a Gauss pseudo–spectral method is employed to determine the minimal power consumption while following the flight trajectory, and particle swarm optimization is used to calculate the optimal battery mass. In the present work, the optimal sizing problem is also discussed. Provided that the field of applicability is restricted to the hovering flight condition of a prescribed empty–operative platform, the discharge model presented in [27] is manipulated to provide the optimal battery capacity as an analytical function of rotorcraft parameters and battery coefficients. Predictions from this model are validated with a few test cases.

The major contribution of the present paper to multirotor aircraft state–of–the–art is the derivation of a fully analytical framework, based on a reduced set of relevant design features, without the need of ad hoc laboratory tests on power plant components and battery packs. Almost all the above mentioned approaches to rotors' performance analysis are, in fact, based on the experimental characterization of the entire propulsion chain (battery, regulator, engine, propeller), with particular focus on aerodynamic analysis. Thus, in order to obtain an accurate estimation of rotorcraft performance as well as a suitable preliminary sizing, the actual power system needs to be selected and available for laboratory test campaign. This makes such approaches not applicable when the platform design process is at an early conceptual stage and the power system selection is the main expected output. To the best of the authors' knowledge, an analytical procedure aimed at accurately estimating the endurance and range of a multirotor platform as a function of a reduced number of design parameters is still missing in the literature. The scope of the present paper is thus to fill this gap by proposing an analytical approach allowing for an accurate and physically consistent estimation of multirotor hovering endurance, based on a limited number of design features, propeller characteristics, and battery parameters. In this respect, the derived closed–form expression for the figure of merit allows for the following three main results: 1) rotorcraft accurate power and endurance prediction at hover, 2) optimal endurance condition analysis, and 3) rotorcraft sizing by providing the optimal battery pack/take–off weight ratio.

The paper is structured as follows. Sections 2 and 3 address the total power required for the hovering flight and the figure of merit characterization, respectively. The analytical framework for multirotor endurance prediction and optimal sizing procedure is derived in Section 4. Numerical simulations and experimental results validating the proposed technique are finally presented Section 5. A section of concluding remarks ends this paper.

2. Power Required at Hover

Consider a multirotor with N identical electric motors and propellers, the latter characterized by a number B of blades. A planar non–ducted non–intermeshing configuration is analyzed where the thrust generated by each rotor is aligned with the local vertical when the vehicle is at hover. Extension to a non–planar configuration is straightforward and can be obtained from the analysis in [6].

The total power required for flight,

$$P_r = P_s + P_h \tag{1}$$

is expressed as the sum of two main contributions [38], namely the power to be absorbed by onboard systems, P_s, and the power necessary for the hovering condition, P_h. The former, allocated to avionics and payload, is assumed to be approximately constant. The latter, related to the generation of thrust, is calculated as $P_h = N\, P_{sh}$, where $P_{sh} = P_{id}/f$ is the power delivered by each electric motor to its rotor shaft, obtained by dividing the ideal induced power P_{id} by the rotor figure of merit $f < 1$. Provided m is the rotorcraft mass and g is the gravitational acceleration, let $W = m\, g$ be the take–off weight. On the basis of momentum theory, $P_{id} = T\, v_i$ is obtained as the product between the thrust generated by the single rotor at hover, $T = W/N$, and the induced speed v_i, assumed to be uniform on the actuator disk. According to Glauert's hypothesis [44], the induced velocity is expressed as a function of rotor thrust, $v_i = \sqrt{T/(2\, \rho\, A)}$, where ρ is air density, $A = \pi\, R^2$ is rotor disc area, and R is rotor radius. The effect of the rotor induced velocity on the airframe drag, which would be included in the computation of P_h, is disregarded in the present framework.

The power output of the battery delivered to the propulsion system is reduced by losses within the electric driving system made of cables, electronic speed controllers (ESCs), and electric motors. Although each element has its own efficiency, η_c, η_{esc}, and η_m, respectively, for the purpose of the present work they are combined into an overall electrical efficiency, $\eta_e = \eta_c\, \eta_{esc}\, \eta_m$, such that

$$\eta_e(P_b - P_s) = P_h \tag{2}$$

where P_b is the total power produced by the battery pack(s). Taking into account Eq. (1) and the definition of P_h, the total power requested from the battery for the hovering flight becomes

$$P_b = P_s + N\, P_{id}/\,(f\,\eta_e) \tag{3}$$

Note that in a correctly sized propulsion system it is $\eta_e \approx \eta_{esc}\,\eta_m$, provided that power losses in cables are typically negligible within the overall efficiency analysis. On the converse, the system made of ESCs and motors represents a significant source of inefficiency, with performance that is a function of angular rate, torque, and applied voltage [45, 46]. In order to perform the correct characterization of η_e, specifications are typically provided by system manufacturers, retrieved from online databases [47, 48], or determined experimentally (see Section 5 for some applicative examples).

3. Figure of merit characterization

The figure of merit characterization is based on a detailed knowledge of the aerodynamic coefficients, whose identification requires complex measurements or calculations. In the present framework, the figure of merit is expressed as function of few propeller parameters that can be extracted either from the propeller datasheet or from simple measurements. Once this expression is identified from basic theoretical considerations, the required correction coefficients are identified that best predict the performance of a class of standard propellers optimized for multirotor applications.

3.1. Blade–element theory analysis

Let Ω be the rotor angular rate, such that $V_{tip} = \Omega\, R$ is blade tip speed, and define the thrust coefficient, $C_T = T/(\rho\, A\, V_{tip}^2)$. The figure of merit, as derived by BET and expressed as a function of C_T, is [39]:

$$f = \frac{\dfrac{C_T^{3/2}}{\sqrt{2}}}{\kappa_{ind}\dfrac{C_T^{3/2}}{\sqrt{2}} + \dfrac{\sigma\, C_d}{8}} \tag{4}$$

where $\sigma = B\,\bar{c}/(\pi\, R)$ is rotor solidity (with B being the number of blades and $\bar{c}$ the blade mean aerodynamic chord), C_d is the airfoil drag coefficient averaged along the blade, and κ_{ind} is the induced–power correction factor. This coefficient is derived from rotor measurements or flight tests and it encompasses a number of non ideal effects, including nonuniform inflow, tip losses, wake swirl and contraction, blades interference, etc. Although κ_{ind} depends on several blade parameters and is a function of C_T for a generic lifting rotor [39], it must be noted that in typical small–scale multirotor applications C_T has limited variability over the available throttle range (see Fig. 3.a), especially at high rotational speed, where the design operating point is typically located [49]. It follows that the resulting small fluctuations of κ_{ind} have a limited impact on the figure of merit. Therefore, in the present model κ_{ind} is fairly assumed as a constant.

On the other hand, the term related to the profile losses has a larger impact at small C_T values. Therefore, the attention is focused on the analysis of the drag coefficient C_d and its detailed expression. To this end, define $\mathrm{Re} = \rho\, c_{75}\, V_{75}/\mu$ as the Reynolds number conventionally evaluated at 75% blade radius [40], where μ is the dynamic viscosity of the air, while c_{75} and

$V_{75} = \sqrt{v_i^2 + (0.75 \cdot V_{tip})^2}$ respectively represent the local airfoil chord and the relative airspeed.

It is important to stress that in large–scale rotors a reasonable first assumption is to consider $C_d = C_{d_0}$, namely a constant independent from Reynolds number, being the flow fully turbulent. Instead, in small–scale rotors, the Reynolds number typically ranges between 10^4–10^5, so that the flow can be assumed to be fully laminar [40] and $C_d = C_d(\mathrm{Re})$. To find an expression for C_d the friction coefficient C_f can be expressed according to Blasius theory as [50]:

$$C_f = 1.328/\sqrt{\mathrm{Re}}. \tag{5}$$

Although Eq. (5) is derived for a flat–plate boundary layer at zero pressure gradient, in this regime the expression

$$C_d = 2\,C_f, \tag{6}$$

obtained considering both sides of the blade–section, results to be a reasonable estimate of the drag coefficient for an airfoil at low angle of attack [51]. Therefore Eq. (6) is implemented in the present model to describe Reynolds number effects on the profile losses. On the other hand, effects such has boundary layer growth and separation are neglected under the assumption that each section of the considered blade is purposely designed to work at a limited angle of attack during a hovering condition.

In order to characterize the local blade air flow, the blade tip speed (and, hence, C_T) needs be estimated for a given thrust condition. According to linearized aerodynamic theory, the local 2–D blade lift coefficient is written as $C_l = C_{l\alpha}\,(\alpha - \alpha_0) = C_{l\alpha}\,(\theta - \alpha_0 - \phi)$, where $C_{l\alpha}$ is the slope of the 2–D lift coefficient, α_0 is the corresponding zero–lift angle, θ is the pitch angle, and ϕ is the relative inflow angle at a generic airfoil section due to the induced flow. Although $C_{l\alpha}$ and α_0 may vary according to the local airfoil characteristics and flow conditions, an average value for both parameters, constant along the blade, is considered. Furthermore, define y as the radial distance from the rotational axis and $r = y/R$ as the non–dimensional location along the blade, such that $r = 0$ at the rotor hub and $r = 1$ at the tip. In this framework, rotor blades are modeled with a linear twist, such that the pitch angle takes the form $\theta(r) = \theta_0 + r\,\theta_{tw}$, where θ_0 is the pitch angle value ideally extrapolated to $r = 0$ and θ_{tw} is the total blade twist angle (tip minus root pitch angle). In Ref. [39] it is shown that, if the reference blade pitch angle (here defined as θ_{75}) is taken at $r = 0.75$, then $\theta(r) = \theta_{75} + (r - 0.75)\theta_{tw}$ and

$$C_T = \frac{1}{2}\sigma\, C_{l\alpha} \left(\frac{\theta_{75} - \alpha_0}{3} - \frac{\lambda}{2} \right) \tag{7}$$

where $\lambda = v_i/V_{tip}$ is rotor inflow ratio. Taking into account Eq. (7) and rewriting the thrust coefficient as $C_T = 2\,(v_i/V_{tip})^2$, it follows:

$$2\left(\frac{v_i}{V_{tip}}\right)^2 = \frac{1}{2}\sigma\, C_{l\alpha} \left(\frac{\theta_{75} - \alpha_0}{3} - \frac{v_i}{2\,V_{tip}} \right) \tag{8}$$

that can be arranged to give

$$2\,\sigma\, C_{l\alpha}\,(\theta_{75} - \alpha_0)\, V_{tip}^2 - 3\,\sigma\, C_{l\alpha}\, v_i\, V_{tip} - 24\, v_i^2 = 0 \tag{9}$$

Assuming V_{tip} as the unknown variable, two real distinct solutions are provided by Eq. (9). After excluding the negative one, the required tip speed, obtained by BET, results to be a function of the induced velocity v_i as

$$V_{tip}^{BET} = k_{tip}\, v_i \tag{10}$$

where

$$k_{tip} = \frac{1}{4}\left(\frac{1+\sqrt{1+\dfrac{64}{\sigma\, C_{l\alpha}}\theta_{75}/3}}{\theta_{75}/3}\right) \tag{11}$$

is obtained by embedding, for simplicity, α_0 into θ_{75} for profile sections with low mean–camber line curvature. Finally, θ_{75} is estimated as

$$\theta_{75} = \arctan\left(\frac{\Gamma}{0.75\cdot\pi\, D}\right) \tag{12}$$

where Γ is nominal blade advance pitch, provided by the manufacturer, that indicates the distance traveled by the propeller in one turn in the absence of slip [52].

By putting together Eqs. (10), (11), and (12), the thrust coefficient in Eq. (7) becomes:

$$C_T = \sigma\,\pi\left(\frac{4\,\Gamma}{9\,\pi\, D} - \frac{1}{2\,k_{tip}}\right) \tag{13}$$

where it is assumed $C_{l\alpha} = 2\,\pi\ \mathrm{rad}^{-1}$ and $\theta_{75} \approx \Gamma/(0.75\cdot\pi\, D)$.

The combination of Eqs. (4), (5), and (13) highlights that, under the assumptions made, the figure of merit nominally depends on two main non–dimensional parameters, namely Γ/D and Re. A third parameter is represented by the solidity ratio σ. However, in typical multirotor applications, σ is found to have a limited variability, with average values in the order of 0.1 for two–bladed configurations [36]. Therefore, in this framework f is considered as a function of two non–dimensional parameters only. The goal is to find an analytical function $H = H(f,\, \Gamma/D,\, \mathrm{Re}) = f\,(\Gamma/D)^{\alpha}\,\mathrm{Re}^{\beta}$ that smoothly fits the experimental data. The appropriate choice of α and β will be made on the basis of an iterative procedure that minimizes the order of the polynomial needed to fit the data (as it will be shown in Section 3.2.2).

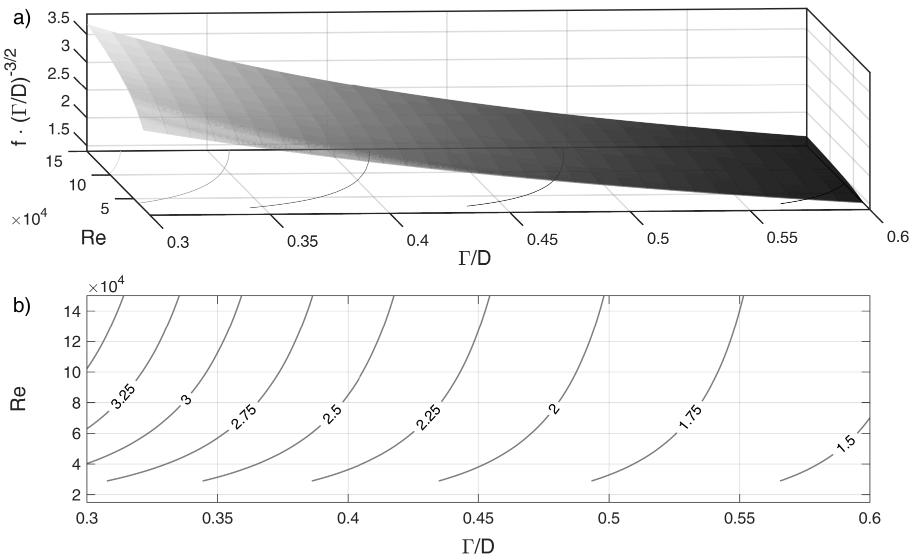

Figure 1: The non–dimensional function $f\,(\Gamma/D)^{\alpha}\,\mathrm{Re}^{\beta}$ as obtained by Eqs. (4), (5), and (13) ($\alpha = -3/2$, $\beta = 0$).

As an example, Fig. 1 shows that for $\alpha = -3/2$ and $\beta = 0$, H is a smooth function of Γ/D and Re. Following Eqs. (4), (5), and (13), the Reynolds number is calculated in standard conditions for a rotation rate Ω in the range $100 - 800$ rad/s. A reference configuration is considered with diameter $D = 15$ in, the value of σ is selected as 0.1, and a constant value of $\kappa_{ind} = 1.25$ is assumed without loss of generality. As the plot shows, the figure of merit increases monotonically with Re. This is a consequence of the monotonic decrease of the drag coefficient with Reynolds number in the range considered here. However, it has to be pointed out that the model in Eq. (10) implies a constant inflow–ratio, with the result that C_T in Eq. (13) does not vary with thrust, for a given value of Γ/D. Conversely, C_T may vary as the Reynolds number increases, due to the increase in angular velocity. This produces a decay of the figure of merit above a certain critical value of

Re, as a consequence of non–ideal flow conditions. This and other effects will be accounted for in the next section, where the ideal model introduced above is re–discussed with the contribution of experimental correction factors.

3.2. Enhanced blade characterization

The general expression for f obtained by Eqs. (4), (5), and (13) is useful to determine the relevant parameters needed to fully describe the figure of merit of a typical multirotor blade. However, this expression is obtained with strong assumptions on the blade and inflow characteristics, such as profile curvature, blade twist configuration, induced velocity distribution, and, in general, all the hypotheses at the base of BET (including the blade spanwise–averaging of aerodynamic properties).

To compensate for these effects, correction factors need to be experimentally determined and introduced in the modeling approach. In this regard, an experimental campaign is conducted with details provided in what follows. All tests are performed on a set of commercial–of–the–shelf propellers, selected on the basis of the following assumption:

Assumption 1 *Static thrust is generated by a two–bladed propeller ($B = 2$) specifically designed for multirotor applications. It is assumed that* $0.3 \leq \Gamma/D \leq 0.6$ *and* $D \leq 16$ *in.*

3.2.1. Experimental setup

A total of 9 different propellers, depicted in Figure 2, is selected with characteristics detailed in Table 1.

For each propeller, a static thrust test is performed by a propulsion system made of a T–Motor T40A ESC and a T–Motor Antigravity 4006 KV380 brushless motor. The unit is mounted on a RCbenchmark Series 1585 thrust

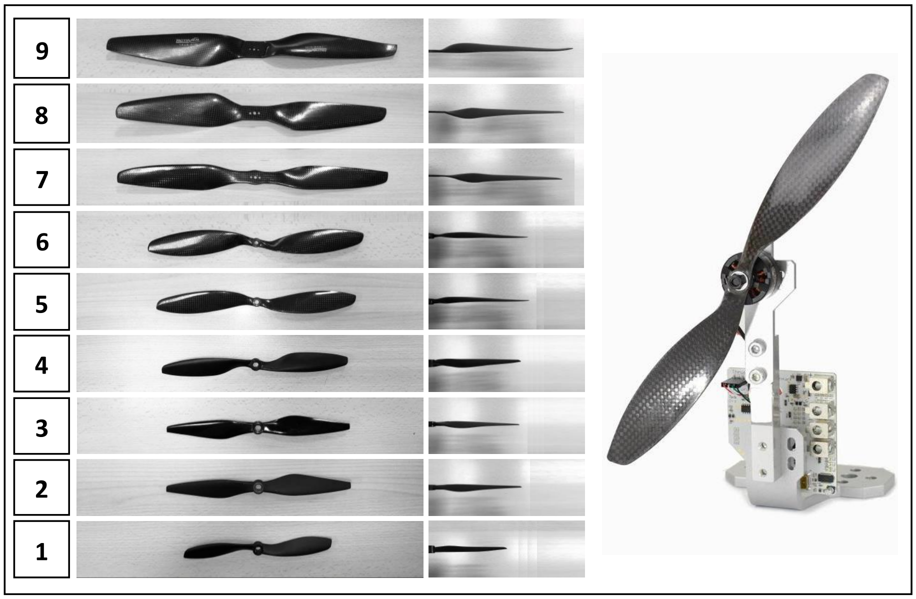

Figure 2: The sample propellers (planform and side views) and a detail of the thrust stand.

stand tailored to small and medium size drone optimization analysis. The test bench supports thrust and torque measurement up to 5 kgf and 1.5 Nm, respectively, and an optical RPM probe for propeller angular rate estimation. The load cells are temperature–compensated and a preliminary calibration procedure allows for accurate measurements over the full operating range. Electrical power required for the propulsion system is delivered by a laboratory power supply stabilized at 24 V DC.

Each experiment is conducted at room temperature $\tau = 24$ °C and static pressure $p = 100\,877$ Pa, with estimated air density $\rho = 1.1827$ kg/m^3 and air dynamic viscosity $\mu = 18.32 \cdot 10^{-6}$ Pa s. Provided that the control signal is obtained by pulse–width modulation (PWM), the throttle command is progressively incremented from 1000 to 1800, respectively generating zero and maximum thrust, with steady–state measurements taken at intervals of 100.

Table 1: Relevant data of tested propellers (CF: carbon fiber, CFRN: carbon fiber reinforced nylon).

	Propeller	Finish	Material	D [in]	Γ [in]	$\bar{c}$ [mm]	c_{75} [mm]
1	DJI 0845	polish	CFRN	8	4.5	17.6	21
2	DJI 1038	polish	CFRN	10	3.8	21.5	18
3	DJI 1038S	glossy	CFRN	10	3.8	21.5	18
4	DJI 1045	polish	CFRN	10	4.5	22.0	24
5	HobbyKing 1147	glossy	CF	11	4.7	25.3	29
6	HobbyKing 1238	glossy	CF	12	3.8	28.4	31
7	RC Timer 1555	glossy	CF	15	5.5	29.3	30
8	RC Timer 1555C	glossy	CF	15	5.5	34.2	30
9	RC Timer 1655	glossy	CF	16	5.5	33.7	31

For each propeller, the test is repeated 3 times in the same conditions and collected data are used to derive a single averaged curve for each measured quantity. In Figure 3 the results obtained for propellers 5 and 7 are reported as an example, showing the measured thrust coefficient C_T, torque Q, and angular rate Ω as a function of PWM command.

3.2.2. Experimental results and fitting parameters

One important aspect of the model derived in Eq. (10) is that of constant inflow ratio. This implies a constant value of C_T for a given value of Γ/D. As mentioned above, this is not verified in practice. Hence, it is first needed to introduce in the proposed model a correction factor that allows for a variation of the inflow–ratio with V_{tip}.

Let ξ be a correction factor to the theoretically estimated tip speed V_{tip}^{BET} in Eq. (10), such that $V_{tip} = \xi\, V_{tip}^{BET}$, where V_{tip} is obtained by direct measurement. In Figure 4 the non–dimensional quantity $g \triangleq \xi \cdot (\Gamma/D)^2/\sigma$ is plotted as a function of Γ/D and the induced speed v_i for all $V_{tip}^{BET} \neq 0$. The

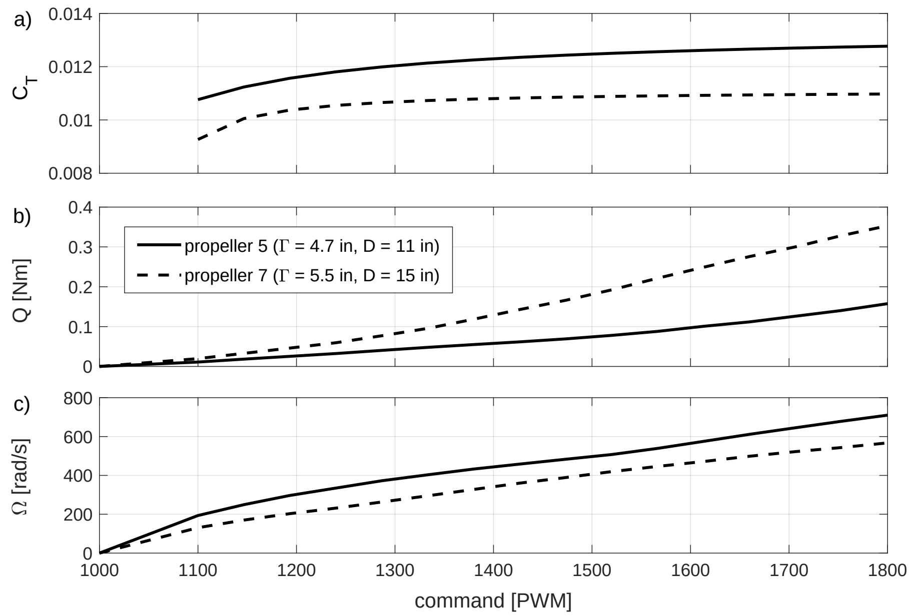

Figure 3: Measurements obtained for propellers 5 and 7.

mathematical form of g, which provides a weight equal to $(\Gamma/D)^2/\sigma$ to the correction factor ξ, is chosen after an iterative procedure aiming at a smooth distribution of experimental data. Data points in Figure 4.a are fitted by the surface $G(\Gamma/D,\, v_i) = [v_1 + v_2 (\Gamma/D)^q] (v_3 + v_4\, v_i^r)$, parametrized by coefficients $v_1 = -9.144 \cdot 10^{-2}$, $v_2 = 2.599$, $v_3 = 2.525$, $v_4 = 7.784 \cdot 10^{-1}$, $q = 1.757$, $r = -5.831 \cdot 10^{-1}$, with root mean square residual equal to 0.054. Taking into account the definition of g, the formulation of the bivariate function $G(\Gamma/D,\, v_i)$ and the preliminary estimation obtained by BET in Eqs. (10)–(12), it is $\xi \approx \sigma\, G/(\Gamma/D)^2$ and the corrected estimate, $\hat{V}_{tip}$, of tip speed is finally written as:

$$\hat{V}_{tip}(v_i) = \xi\, V_{tip}^{BET} = \frac{k_{tip}\,\sigma}{(\Gamma/D)^2} [v_1 + v_2 (\Gamma/D)^q] (v_3 + v_4\, v_i^r)\, v_i. \tag{14}$$

After characterizing the blade local flow condition, Eq. (4) is discussed on an experimental basis. For each test, the figure of merit is calculated as

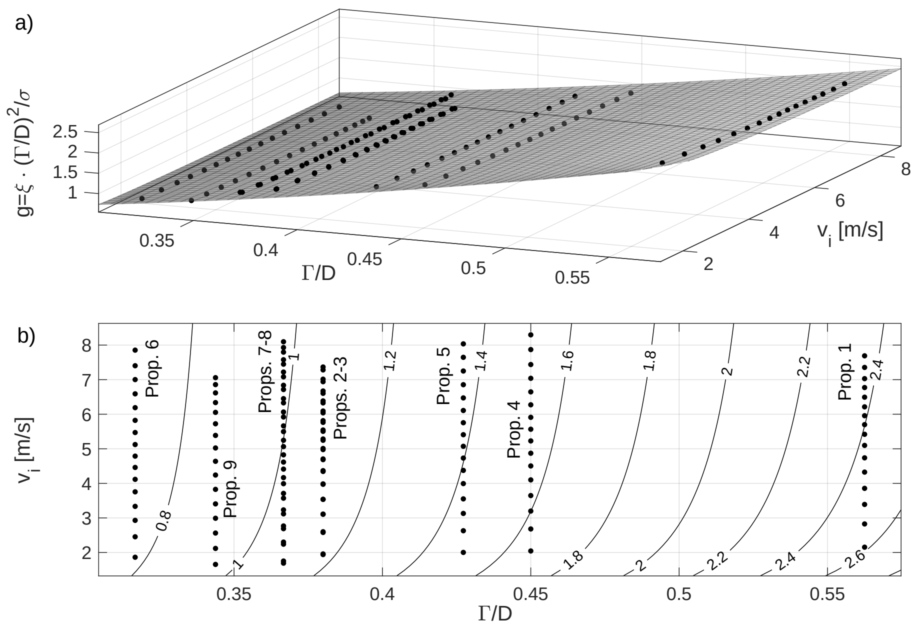

Figure 4: The non–dimensional function g for the complete set of propellers: a) measured data points and fitting surface; b) contour plot with corresponding iso–response lines.

$f = P_{id}/P_{sh}$, according to the definition given in Section 2, provided $P_{sh} = Q\,\Omega$ is derived from the product between the measured torque Q and the angular rate Ω. Based on experimental results, the non–dimensional quantity $h \triangleq f \cdot (\Gamma/D)^{\alpha}$, defined in Section 3.1, is plotted in Figure 5 as a function of Γ/D and the Reynolds number Re, with the fitting parameters selected as $\alpha = -2$ and $\beta = 0$. Data points in Figure 5.a are fitted by a second–order polynomial surface, represented by the bivariate function $H\,(\Gamma/D,\,\mathrm{Re}) = f_{00} + f_{10}\,(\Gamma/D) + f_{01}\,\mathrm{Re} + f_{20}\,(\Gamma/D)^2 + f_{11}\,(\Gamma/D)\,\mathrm{Re} + f_{02}\,\mathrm{Re}^2$, with coefficients $f_{00} = 17.03$, $f_{10} = -56.28$, $f_{20} = 50.61$, $f_{01} = 5.19 \cdot 10^{-5}$, $f_{11} = -6.034 \cdot 10^{-5}$, $f_{02} = -1.033 \cdot 10^{-10}$, and root mean square error residual equal to 0.072. Taking into account the definition of h and the formulation adopted for $H\,(\Gamma/D,\,\mathrm{Re})$, it follows that the estimated figure of merit, $\hat{f}$, is expressed as

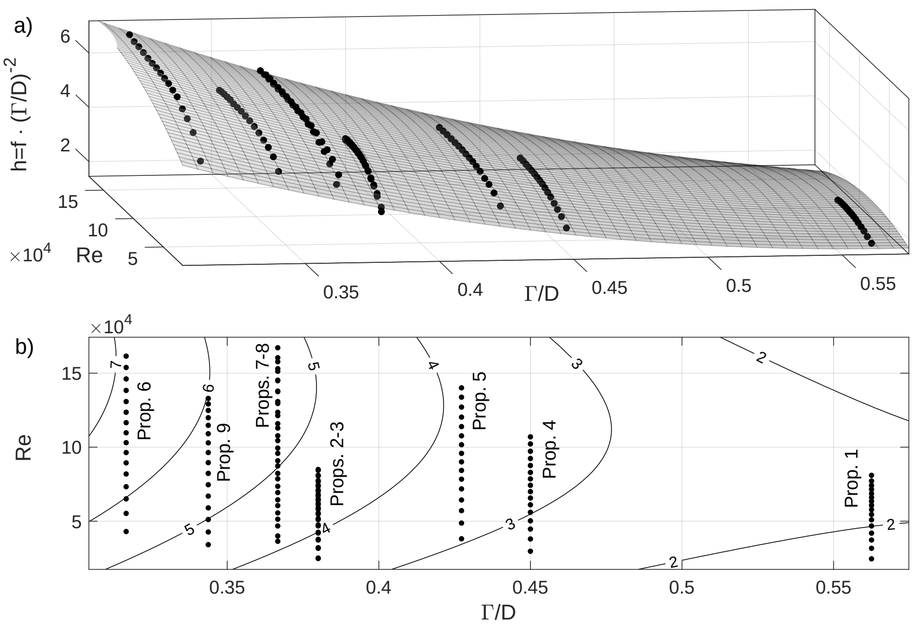

Figure 5: The non–dimensional function h for the complete set of propellers: a) measured data points and fitting surface; b) contour plot with corresponding iso–response lines.

a function of Reynolds number according to the model

$$\hat{f}\,(\mathrm{Re}) = f_0 + f_1\,\mathrm{Re} + f_2\,\mathrm{Re}^2 \tag{15}$$

where

$$f_0 = (\Gamma/D)^2\left[f_{00} + f_{10}\,(\Gamma/D) + f_{20}\,(\Gamma/D)^2\right] \tag{16}$$

$$f_1 = (\Gamma/D)^2\left[f_{01} + f_{11}\,(\Gamma/D)\right] \tag{17}$$

$$f_2 = (\Gamma/D)^2\,f_{02} \tag{18}$$

Remark 1. The results derived in terms of figure of merit characterization and tip speed estimation are valid under Assumption 1, characterizing a particular class of propellers. In what follows, the field of applicability is discussed. First of all, commercial–off–the–shelf components are considered, optimized for multirotor vehicles. Then, the hobby and recreational applications are excluded, where the use of very small propellers ($D < 8$ in, often tri/four–bladed) is widespread and determines high–agility racing capabilities, thanks to the lower rotor inertia and small blade pitch angle.

With regard to professional applications, where the focus is posed on stability and endurance capabilities, it is interesting to note where the most important drone and propellers manufacturers targeted the market. In Table 2, for example, the complete multirotor fleets of some of the main professional drone companies are listed, with relevant data characterizing the maximum take–off mass (MTOM) and the adopted propellers for 18 different products [53, 54, 55]. The applications range from aerial photography and videography, 3D mapping, surveying, and environment monitoring, to precision farming and crop spraying. Taking a look at the types of propellers, it can be noted that 15 samples are characterized by $0.3 \leq \Gamma/D \leq 0.6$ and 9 of these have a diameter $D < 16$. The result is that 50% of all the considered platforms satisfy the requirements in Assumption 1 (the same percentage increases to 100% for multirotors with $MTOM \leq 6$ kg). In addition to the analysis of existing vehicles, it is interesting to investigate how the spare market of multirotor components is structured, provided that the design of novel platforms typically requires a wide spectrum of available propeller configurations.

To this aim, the complete catalogs of two of the biggest propellers manufacturers/resellers was dissected [56, 57]. In particular, a total of 89 propellers was investigated, characterized by a different diameter, pitch, material, finish, and blade shape. Results are reported in Figure 6. It can be noted that 78% of propellers satisfies the constraint on rotor diameter ($D < 16$ in) while 93% complies with $0.3 \leq \Gamma/D \leq 0.6$. Summarizing, 71% of collected samples

Table 2: DJI, Freefly, and Yuneec multirotors with relevant data (the symbol 'F' in the fourth column is related to foldable blade configurations).

Multirotor	$MTOW$ [kg]	N	B	Γ [in]	D [in]	Γ/D
DJI						
Mavic Mini 2	0.242	4	2F	2.6	4.7	0.553
Mavic Air 2	0.570	4	2F	3.8	7.2	0.528
Mavic 2	0.906	4	2F	4.3	8.7	0.494
Phantom 4 PRO	1.388	4	2	5.5	9.4	0.585
Inspire 2	4.250	4	2	5	15	0.333
S800 EVO	8	6	2F	5.2	15	0.347
S1000	11	8	2F	5.2	15	0.347
Matrice 200 V2	6.140	4	2	6	17	0.353
Matrice 300 RTK	9	4	2F	10	21	0.476
Matrice 600 PRO	15.5	6	2F	7	21	0.333
MG–1P	24.5	8	2F	7	21	0.333
AGRAS T16	42	6	2F	9	33	0.273
AGRAS T20	47.5	6	2F	9	33	0.273
Freefly Systems						
Astro	8.382	4	2F	7	21	0.333
Alta–8	18.1	8	2F	6	18	0.333
Alta–X	34.86	4	2F	9	33	0.273
Yuneec						
Typhoon H520	1.633	6	2	5.7	9.8	0.582
Typhoon H3	2	6	2	5.7	9.8	0.582

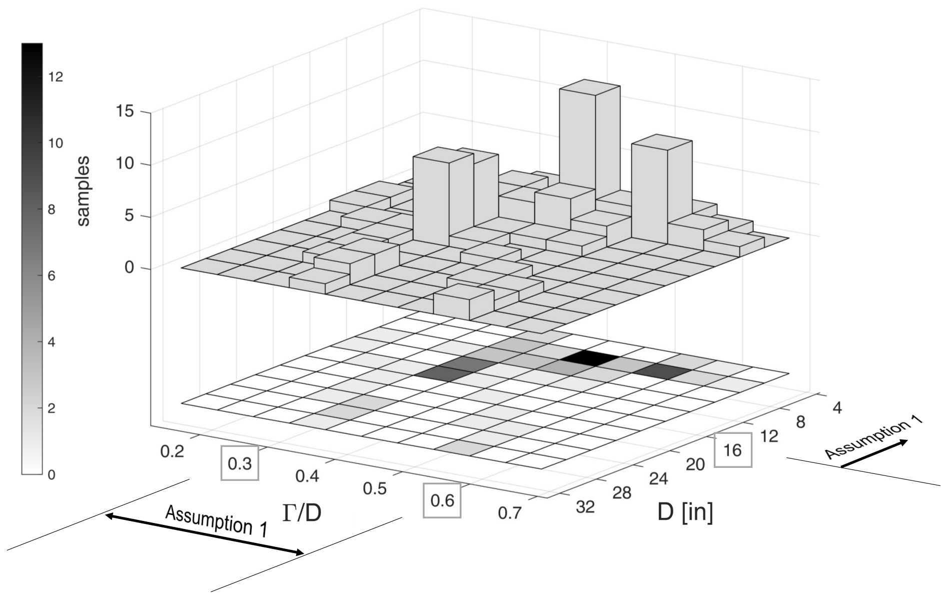

Figure 6: Bivariate histogram analysis of RC Timer and T–Motor propellers for professional multirotor applications.

falls under the requirements of Assumption 1.

It is thus shown that the proposed approach fits a wide applicability range, provided that the considered class of propellers is a reference for customized or off-the–shelf small–scale platforms. On the other hand, it must be noted that such a market trend is also representative of all the cases where high lifting capabilities are required but thrust is preferably distributed into a higher number of smaller rotors. Despite the inherent increase of ideal induced power, the adoption of such configurations is widespread and allows 1) the design of compact platforms, 2) the reduction of eventual damages caused by blade impacts, 3) a higher degree of residual controllability after failure of one or more propulsive units, and 4) reduced sensitivity to external disturbances. In this respect, electrical and mechanical performance data for a comprehensive range of motor and propeller combinations are reported in

[36], with a detailed statistical analysis.

4. Performance analysis and optimization

4.1. Hover endurance prediction

Consider the expression obtained in Eq. (3) and note that, for a multirotor in a hovering condition, battery power is a constant. In Ref. [27] a novel formulation for constant–power battery discharge process is proposed, where discharge time is expressed as a function of discharged capacity and absorbed power. Let $I = I(t)$ be the current provided by the battery pack at time t and $C = C(t)$ be the discharged capacity, obtained as

$$C(t) = \int_0^t I(s)\,ds \tag{19}$$

Provided $P_b > 0$, the discharge process is stopped at time t_f when $C_f = C(t_f) = K\,C_0$, with C_0 equal to the nominal battery capacity and $K < 1$ being a predefined discharge percentage. Discharge time is expressed in the form

$$t_f = \delta\,P_b^{\epsilon}\,C_f^{\beta} \tag{20}$$

where coefficients $\delta > 0$, $\epsilon < -1$, and $0 < \beta < 1$, which depend on battery technology, ambient temperature, and number of series–connected cells, are determined experimentally. Conversely, when power is delivered by Li–Po battery packs and no equipment is available to perform ad hoc battery tests, the analytical results derived in [27] can be adopted, especially at a preliminary design stage. In particular, let N_s be the number of series–connected cells and define δ_0, ϵ_0, and β_0 as battery coefficients at the reference ambient temperature, $\tau_0 = 23$ °C. It is:

$$\delta_0(N_s) = -0.1067\, N_s^3 + 0.8960\, N_s^2 + 2.488\, N_s + 0.6299 \tag{21}$$

$$\epsilon_0(N_s) = 2.917 \cdot 10^{-4}\, N_s^3 - 1.375 \cdot 10^{-3}\, N_s^2 + 3.083 \cdot 10^{-3}\, N_s - 1.041 \tag{22}$$

while $\beta_0 = 0.9664$. In general, the parameters that define the variation of δ_0 and ϵ_0 as a function of N_s depend on battery technology and aging. With this in mind, it is pointed out that the experiments at the base of Eqs. (21) and (22) were performed on battery packs with exactly the same technology, at approximately half of their operational lifespan, as a compromise between better performance (when the battery pack is new) and degraded conditions. Of course, an accurate estimate of discharge time would require to repeat the whole experimental campaign at various stages of battery life, in order to estimate the updated parameters and the effective capacity as battery aging and degradation develop. This can be performed according to the procedure in [27] by means of an electronic load or by collecting flight data in terms of both hour–integral discharged capacity and delivered power, for different loading conditions. Anyway, to the authors' experience with Li–Po batteries, the trends of $\delta_0(N_s)$ and $\epsilon_0(N_s)$ are correctly evaluated, with only minor variations.

In Ref. [27] an experiment was also conducted to investigate the effect of environment temperature on battery performance. In the present framework, the analyzed trend is extrapolated by assuming a linear regression, based on the available experimental data respectively obtained at 23 °C and at a lower temperature, namely 17 °C. Provided $\Delta\tau = \tau - \tau_0$ is the temperature variation with respect to the reference case, the environment–compensated battery parameters are expressed as a function of N_s and $\Delta\tau$ as

$$\delta(N_s,\,\Delta\tau) = \delta_0(N_s)\,(1 - c_1\,\Delta\tau) \tag{23}$$

$$\epsilon(N_s,\,\Delta\tau) = \epsilon_0(N_s)\,(1 - c_2\,\Delta\tau) \tag{24}$$

$$\beta(\Delta\tau) = \beta_0\,(1 - c_3\,\Delta\tau) \tag{25}$$

where $c_1 = 0.0046$ 1/°C, $c_2 = 0.0024$ 1/°C, and $c_3 = 0.0011$ 1/°C are correction coefficients.

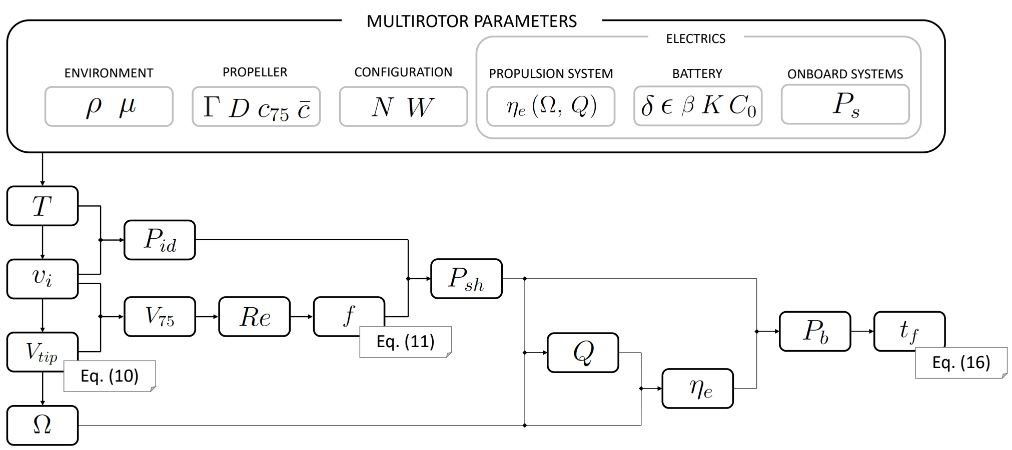

Figure 7: The proposed procedure to estimate battery power and flight time for a multirotor at hover.

In Figure 7 the complete procedure necessary to estimate the hovering flight time for a given multirotor configuration is detailed. The set of parameters that are required to be measured or estimated a priori are reported at the top of the same figure. For a given take–off weight and multirotor configuration, the required thrust T of the single rotor is used to derive the induced speed v_i and the corresponding ideal induced power P_{id}. By Eq. (14) one estimates the corrected blade tip speed and the Reynolds number at 75% blade radius, such that the figure of merit can be calculated according to the experimental model in Eqs. (15)–(18). Given the ideal power P_{id}, corrected by the figure of merit to the shaft power P_{sh}, it is possible to characterize the torque $Q = P_{sh}/\Omega$ applied by the electric motor to its rotor and the efficiency η_e of the electric propulsion system at that operating point. As a final step, the total battery power is derived as in Eq. (3), provided the power necessary for onboard systems P_s is known. The hovering time follows from Eq. (20) for a prescribed percentage of the nominal battery capacity C_0, in the considered environmental conditions.

4.2. Sizing of battery capacity

In this section, the optimal value of the battery capacity that maximizes hover endurance is determined, following an approach similar to that described in [20], where the optimal battery pack configuration was obtained by using the classical Peukert discharge model. For the aim of the present analysis, the total take–off weight is conveniently decomposed into

$$W = W_b + W_0 \tag{26}$$

where W_b is the battery weight and W_0 is the operative empty weight made of contributions from: a) the frame (structure and rigging), b) the propulsive system (motors, electronic speed controllers, and propellers), c) the avionics (autopilot and communication system), and d) the eventual payload equipments. Let $\chi = W_b/E_0 = W_b/\left(\mathcal{V}_0\, C_0\right)$ indicate the nominal battery weight/energy ratio (that is, the inverse of battery energy density), such that the aircraft total weight in Eq. (26) can be rewritten as

$$W = W_0 + \chi\, \mathcal{V}_0\, C_0 \tag{27}$$

where $\mathcal{V}_0$ is battery nominal voltage. Rotorcraft sizing is thus performed assuming take–off weight W as the independent variable in Eqs. (3) and (14), and determining battery capacity from Eq. (27),

$$C_0 = \frac{W - W_0}{\chi \, \mathcal{V}_0} \tag{28}$$

Given a predefined discharge percentage $K \leq 1$, flight endurance is thus estimated according to Eq. (20) as a function of take–off weight W and, hence, of rated capacity C_0.

The necessary condition for the optimal value of W which maximizes the hovering flight time t_f (that is, the best endurance weight configuration, $W = W_{be}$) is obtained by solving the equation $dt_f/dW = 0$. The sign of the first derivative before and after its zeros (or, equivalently, the sign of the second derivative at the zeros) allows for identifying maxima and minima of the endurance curve. Despite the analytical formulation derived in Section 3 for the figure of merit characterization, it is clear that, in the most general case, the propulsive system efficiency η_e is a function of the estimated rotor angular rate Ω and applied torque Q, which is estimated from vehicle datasheet or determined experimentally. Hence, an analytical solution for the equation $dt_f/dW = 0$ (and the sign of d^2t_f/dW^2) with general validity is not available. An iterative root search algorithm, such as Newton–Raphson scheme [58], needs to be implemented and the second derivative at the zero can be evaluated by means of centered differences. As an alternative, the function that relates W to the expected performance in Eq. (20) can be plotted and the best weight configuration identified either graphically on the plot or numerically by means of a search algorithm, such as the parabolic search or the simplex method [59].

An approximate closed–form solution, $W^\star_{be}$, to the optimal sizing problem can be made available on the basis of the following simplifying assumptions: 1) η_e is a constant; 2) the power required for avionics and payload is negligible with respect to the power delivered to the propulsion system, namely $P_s \ll N\,P_{sh}$; 3) the required blade tip speed is simply estimated on the basis of BET according to Eq. (10), where $V_{tip}^{BET} = k_{tip}\,v_i$, with no correction; 4) the effect of induced flow on local blade airspeed computation is disregarded, that is to say $v_i \ll 0.75 \cdot V_{tip}$ and $V_{75} \approx 0.75 \cdot V_{tip}$; 5) an ideal battery is considered where discharge time is obtained by Eq. (20) with $\epsilon = -1$ and $\beta = 1$. Taking into account the assumptions given above, the expression dt_f/dW results to be proportional to a fourth order polynomial and $dt_f/dW = 0$ if

$$q_0 + q_1\,y + q_2\,y^2 + q_4\,y^4 = 0 \tag{29}$$

where $y = \sqrt{W}$ and

$$q_0 = 96\,\mu^2\,f_0\,A\,N\,W_0 \tag{30}$$

$$q_1 = 24\,\mu\,c_{75}\,f_1\,k_{tip}\,W_0\sqrt{2\,\rho\,A\,N} \tag{31}$$

$$q_2 = 9\,c_{75}^2\,f_2\,k_{tip}^2\,W_0 - 32\,\mu^2\,f_0\,A\,N \tag{32}$$

$$q_4 = 9\,c_{75}^2\,f_2\,k_{tip}^2 \tag{33}$$

are constant coefficients. Based on Eqs. (16)–(18), it is $f_0\,,f_1 > 0$ and $f_2 < 0$ for all propellers selected under Assumption 1, with the result that $q_0 > 0$, $q_1 > 0$, $q_2 < 0$, and $q_4 < 0$. The sequence of signs in Eq. (29) is thus $++--$, which indicates that, according to Descartes' rule [60], there is only one real positive solution, in the form:

$$W^\star_{be} = {y^\star_{be}}^2 = \left(S + \frac{1}{2}\sqrt{-4\,S^2 - \frac{2\,q_2}{q_4} - \frac{q_1}{q_4\,S}}\right)^2 \tag{34}$$

where

$$S = \frac{1}{2}\sqrt{-\frac{2\,q_2}{3\,q_4} + \frac{1}{3\,q_4}\left(Q + \frac{\Delta_0}{Q}\right)} \tag{35}$$

$$Q = \sqrt[3]{\frac{\Delta_1 + \sqrt{\Delta_1^2 - 4\,\Delta_0^3}}{2}} \tag{36}$$

$$\Delta_0 = q_2^2 + 12\,q_4\,q_0 \tag{37}$$

$$\Delta_1 = 2\,q_2^3 + 27\,q_4\,q_1^2 - 72\,q_4\,q_2\,q_0 \tag{38}$$

Provided that the polynomial in Eq. (29) grows towards $-\infty$ as $y \to +\infty$, the first derivative is expected to be positive before the root and negative after it, thus indicating that the zero of the first derivative corresponds to a maximum for t_f. Finally, the optimal value of the battery capacity that maximizes hover endurance is obtained from Eq. (28) with $W = W_{be}^{\star}$.

5. Results

The proposed technique, developed to estimate the hovering performance of multirotor platforms and to provide battery–sizing guidelines, is numerically validated. In particular, a comparison is provided between model–predicted data and the results of flight tests, in terms of required battery power and hovering endurance. Flight data are provided by the rotorcraft manufacturers (see configurations MR1, MR2, and MR3) or are obtained from a dedicated experimental campaign, performed by the authors at the University of Bologna premises (platforms MR4 and following).

5.1. Battery power prediction

In the present section, four different existing platforms are analyzed (respectively named $MR1$, $MR2$, $MR3$, and $MR4$), with MTOM ranging from about 1.3 to 25 kg and propeller diameter from 9 to 21 in. Battery power is predicted according to the proposed approach and compared with the results of flight data. Main results are then summarized in Table 3.

5.1.1. MR1: DJI Spreading Wings S1000

The DJI Spreading Wings S1000 is characterized by $N = 8$ rotors, each provided with a two–bladed folding CF propeller with $D = 15$ in and $\Gamma = 5.2$ in. Dihedral and tilt angles are, respectively, $\psi = 8$ deg and $\phi = 3$ deg, provided the same nomenclature and definitions of [6] are adopted. Power is delivered by a Li–Po battery pack with $N_s = 6$ series–connected Li–Po cells, through an integrated system made by a proprietary 40 A ESC and a 4114–PRO brushless electric motor with speed constant $k_v = 400$ rpm/V. With a take–off mass $m = 9.5$ kg, the total battery power as measured by the manufacturer is equal to 1 500 W [53].

In the given configuration, the thrust required by the single rotor is $T = W/(N \cos\psi \cos\phi) = 11.78$ N, which produces an induced flow with speed $v_i = 6.49$ m/s and rotor ideal power $P_{id} = 76.5$ W, assuming sea–level standard atmospheric conditions ($\tau = 15$ °C, $\rho = 1.225$ kg/m^3, and $\mu = 1.789 \cdot 10^{-5}$ Pa s). Provided $\bar{c} = 0.0175$ m, the considered propeller is characterized by solidity $\sigma = 0.0586$ while the nominal pitch angle at 75% radius is $\theta_{75} = 0.1461$ rad, according to Eq. (12). Based on BET analysis, the estimated blade tip speed in Eq. (10) is $V_{tip}^{BET} = 135.85$ m/s, with $k_{tip} = 20.92$. Given $\Gamma/D = 0.347$, the corrected tip speed by Eq. (14) is $\hat{V}_{tip} = 57.75$ m/s (corresponding to $\Omega = 303.2$ rad/s). At the considered operating point it is $V_{75} = 43.80$ m/s (which approximately equals the quantity $0.75 \cdot \hat{V}_{tip} = 43.31$ m/s) and the Reynolds number is Re = 56 980, provided

$c_{75} = 0.019$ m is the local chord length. The figure of merit is estimated from the model in Eq. (15) as $f = 0.605$, provided the coefficients in Eqs. (16)–(18) are $f_0 = 0.4329$, $f_1 = 3.726 \cdot 10^{-6}$, and $f_2 = -1.241 \cdot 10^{-11}$. The single rotor shaft power is thus $P_{sh} = P_{id}/f = 126.4$ W, the total power required to hover is $P_h = N\,P_{sh} = 1\,010.9$ W, and the torque applied to the propeller by the electric motor is $Q = P_{sh}/\Omega = 0.417$ Nm. Assuming no payload is powered by the main battery pack, the only contribution to P_s is provided by the avionics. Based on the statistical analysis performed in [61] on DJI products, it is assumed $P_s = 5$ W, which accounts for the current absorbed by the onboard computer and the electric driving system, when no thrust is generated. The electric propulsion system is characterized by DriveCalc on-line computation tools [48]. In particular, the system made of the considered ESC and motor is outlined from the available component database and the overall electric efficiency is evaluated exactly at the given operating point, where $\eta_e = 0.68$. Taking into account Eq. (3), the total power requested from the battery for the hovering flight is $P_b = 1\,492.3$ W, with an estimation error $\varepsilon_P = -0.51\%$ with respect to the nominal value.

5.1.2. MR2: DJI AGRAS MG–1P

The procedure described above is applied to another professional platform for which DJI provides some flight data, namely the AGRAS MG–1P, engineered for agricultural spraying activities. The platform has $N = 8$ rotors, each provided with a two–bladed folding CF propeller with $D = 21$ in, $\Gamma = 7$ in, $\bar{c} = 0.029$ m, and $c_{75} = 0.021$ m (configuration not compliant to Assumption 1). The rotor configuration is planar, except for the tilt angle $\phi = 3$ deg, and thrust is provided by an integrated DJI system made of a 25 A ESC and a 6010 brushless electric motor. Energy is delivered by a MG–12000P Li–Po Intelligent Flight Battery with nominal voltage $\mathcal{V}_0 = 44.4$ V ($N_s = 6$) and capacity $C_0 = 12$ Ah. The total electric power measured during a stable hovering condition is 3 250 W when the take–off mass is $m = 22.5$ kg [53].

In the same condition, the predicted shaft power required to hover is $P_{sh} = 309.0$ W, with the figure of merit being $f = 0.635$, and the torque is $Q = 1.16$ Nm. The overall electric efficiency at the considered operating point is retrieved from the curves provided by the manufacturer in [62] and is equal to $\eta_e = 0.81$. With respect to the systems power consumption, some optimistic data are reported in [32], where avionics (10 W) and payload (40 W) are taken into account for a non–specified spraying mode of pesticides and fertilizers. Taking into account the presence of the onboard high precision radar module (12 W), it follows $P_s = 62$ W and the total power requested from the battery is $P_b = 3\,114.3$ W, with a prediction error equal to -4.18%.

5.1.3. MR3: DJI Phantom 4 V2.0

A small rotorcraft, identified as a study case in [63], is analyzed with characteristics similar to the DJI Phantom 4 V2.0 (reference drone). The platform has $N = 4$ rotors with two–bladed 9×4.5E APC propellers ($D = 9$ in, $\Gamma = 4.5$ in, $\bar{c} = 0.019$ m, $c_{75} = 0.022$ m), designed for fixed–wing electric aircraft (thus partially disregarding Assumption 1). Dihedral and tilt angles, not specified in [63], are assumed to be equal to the reference drone, for which $\psi = 8$ deg and $\phi = 3$. Power is delivered by a Li–Po battery with nominal voltage $\mathcal{V}_0 = 14.8$ V ($N_s = 4$) and capacity $C_0 = 5.9$ Ah. Propulsion is obtained by a set of 12 A ESCs and Flyduino X2208 brushless motors. With a take–off mass $m = 1.375$ kg, each ESC requires 39 W of electrical power at hover, the torque delivered by the electric motor to its propeller is 0.05 Nm at 5 600 rpm, and the shaft power is equal to 31 W. Assuming $P_s = 5$ W [61], the total battery power is thus $(39 \cdot 4) + 5 = 161$ W, according to [63].

Given $\Gamma/D = 0.5$ and $\sigma = 0.106$, the estimated rotor angular rate is $\Omega = 554.8$ rad/s (5 298 rpm), with an error equal to -5.39% with respect to the indicated value. A figure of merit $f = 0.644$ is determined, and the predicted shaft power is $P_{sh} = 30.8$ W (estimation error: -0.65%). The torque results to be $Q = 0.056$ Nm (estimation error: $+11.2\%$) and, based on the efficiency curves provided by the authors in [63], the propulsion system is characterized by $\eta_e = 0.79$. The required electrical power for each ESC is 38.9 W (estimation error: -0.26%) and the total power requested from the battery for the hovering flight is $P_b = 160.5$ W (estimation error: -0.31%).

5.1.4. MR4: DJI Spreading Wings S800 EVO

The proposed method is also validated by means of flight tests performed by the authors at the University of Bologna premises. A DJI Spreading Wings S800 EVO is considered, characterized by $N = 6$ rotors and the same propulsion system analyzed for the DJI S1000 in Section 5.1.1. Dihedral and tilt angles are, respectively, $\psi = 8$ deg and $\phi = 3$ deg and power is delivered by a Tattu 25C battery made of $N_s = 6$ series–connected Li–Po cells with nominal voltage $\mathcal{V}_0 = 22.2$ V and capacity $C_0 = 22$ Ah. The empty operative mass is 4 kg and the considered battery weighs 2.509 kg, such that the take off mass is $m = 6.509$ kg and the thrust required from the single rotor is $T = 10.76$ N. A hovering flight test was performed at the ambient temperature $\tau = 15$ °C and pressure $p = 98\,460$ Pa, with estimated air density $\rho = 1.1904$ kg/m^3 and dynamic viscosity $\mu = 1.789 \cdot 10^{-5}$ Pa s. Taking

Table 3: Analyzed multirotor platforms and battery power prediction errors.

Multirotor	Mass [kg]	N	D [in]	Γ [in]	f	η_e	P_b est. [W]	P_b meas. [W]	ε_P [%]
MR1	9.5	8	15	5.2	0.605	0.68	1 492.3	1 500	-0.51
MR2	22.5	8	21	7	0.635	0.81	3 114.3.3	3 250	-4.18
MR3	1.375	4	9	4.5	0.644	0.79	160.5	161	-0.31
MR4	6.509	6	15	5.2	0.597	0.85	833.4	828.2	0.63

into account the information obtained in flight by averaging the readings of a wattmeter sensor, the measured power resulted to be 828.2 W.

According to the proposed prediction method, the shaft power required to hover is $P_{sh} = 113.4$ W and the torque is $Q = 0.39$ Nm, with the figure of merit being $f = 0.597$. The electric propulsion system is characterized by DriveCalc online computation tool [48], according to which $\eta_e = 0.85$. The only contribution to P_s is provided by the avionics, made of the onboard computer and telemetry system. Based on the statistical analysis performed in [61], it is assumed $P_s = 5$ W and the estimated total power delivered by the battery pack is $P_b = 833.4$ W. In this case, the error of the proposed technique for predicting battery power is only +0.63% with respect to obtained measurement.

5.2. Flight endurance and sizing procedure validation

In what follows, two test cases are analyzed. While addressing the validity of the battery power estimation method, endurance tests allow to address the flight time prediction problem presented in Section 4.

5.2.1. MR5: UNIBO MDV–X4 Multirotor

The first case is represented by the analysis of a rotorcraft with $N = 4$ planar rotors, developed at the University of Bologna (platform MR5, see

Figure 8: The quadcopter MDV–X4 developed at the University of Bologna (MR5).

Figure 8). Power is delivered by the parallel connection of 2 Tattu 25C Li–Po batteries with the same specifications reported in Section 5.1.4, such that $\mathcal{V}_0 = 22.2$ V, and the nominal capacity is $C_0 = 22 \cdot 2 = 44$ Ah. Propulsion is obtained by a set of T–Motor U8 motors with $k_v = 135$ rpm/V [64], driven by T60A electronic controllers, and CF propellers by T–Motor with $D = 29$ in, $\Gamma = 9.5$ in, $\bar{c} = 0.057$ m, and $c_{75} = 0.055$ m (configuration not compliant to Assumption 1). The empty operative mass is 4.245 kg and the considered battery pack weighs $2.509 \cdot 2 = 5.018$ kg, with the result that the take off mass is $m = 9.263$ kg and the thrust required from the single rotor is $T = 22.71$ N. Three hovering flight tests were performed at the ambient temperature $\tau = 22$ °C and pressure $p = 98\,650$ Pa, with estimated air density $\rho = 1.1644$ kg/m^3 and dynamic viscosity $\mu = 1.822 \cdot 10^{-5}$ Pa s. During each flight, the battery pack was discharged to the 80% of nominal capacity, that is to say $C_f = K\,C_0 = 0.8 \cdot 44 = 35.2$ Ah, starting from an initial fully–charged condition. The average values of the measured battery power P_b and flight time t_f resulted to be 703.7 W and 60.4 min, respectively.

Based on the available data, the predicted rotor angular rate is $\Omega = 171.4$ rad/s. The shaft power required to hover is $P_{sh} = 154.4$ W, with the figure of merit being $f = 0.7$ at $\mathrm{Re} = 154\,853$. The efficiency of the electric propulsion system is retrieved from [47], where $\eta_e = 0.88$. No power–consuming payload is carried on board and the avionics is represented by a DJI Wookong–M system, for which $P_s = 5$ W. The predicted power required from the battery pack is $P_b = 707.1$ W (estimation error: +0.48%). Hovering endurance is estimated by Eq. (20), where $\delta = 25.07$, $\epsilon = -1.011$, and $\beta = 0.9675$ are the temperature–compensated battery coefficients, obtained from Eqs. (21)–(25). Predicted flight time is 61.3 min, with an estimation error of +1.49%.

5.2.2. MR6/7/8/9: DJI F550 Flame Wheel

The battery–sizing procedure described in Section 4.2 is experimentally investigated for a DJI F550 Flame Wheel planar hexarotor ($N = 6$), where propulsion is provided by a set of DJI Opto 30A ESCs and DJI 2212 brushless motors. The nominal empty operative mass is 1.35 kg, which includes the contribution of computer and telemetry system, based on a Pixhawk PX4 board with power absorption $P_s = 5$ W. In order to calculate the battery weight/energy ratio to be used during the design process, a reference 25C Li–Po battery by Tattu is considered with nominal voltage $\mathcal{V}_0 = 14.8$ V ($N_s = 4$), capacity $C_0 = 9$ Ah, and mass 0.810 kg ($W_b = 7.94$ N), with the result that $\chi = W_b / (\mathcal{V}_0\, C_0) = 0.0596$ N/(Wh).

The propulsion system made of ESC and motor was previously characterized over an adequate range of angular rate and torque by the RCbenchmark thrust stand at room temperature $\tau = 24$ °C, with voltage stabilized at 14.8 V. Adopting the same procedure described in Section 3, static thrust tests were thus performed on three sample propellers (the same marked as 1, 2, and 4 in Table 1) and the data relative to the measured torque, angular rate, and electrical power were collected. Provided that the electrical efficiency is calculated as the ratio between the available shaft power and the absorbed electrical power, obtained results are reported in Figure 9. Data

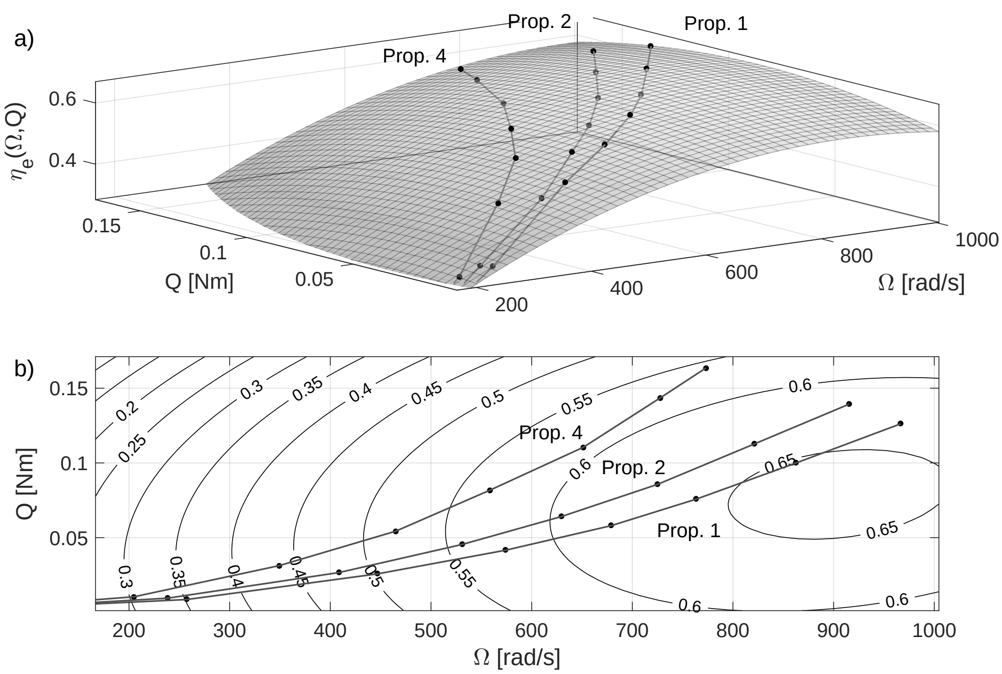

Figure 9: Electrical efficiency of a DJI 2212 brushless motor with DJI Opto 30A ESC: a) measured data points and fitting surface; b) contour plot with corresponding iso–response lines.

points in Figure 9.a are fitted by a second–order polynomial surface, such that $\eta_e\,(\Omega,\,Q) = p_{00} + p_{10}\,\Omega + p_{01}\,Q + p_{20}\,\Omega^2 + p_{11}\,\Omega\,Q + p_{02}\,Q^2$, with coefficients $p_{00} = 7.145 \cdot 10^{-2}$, $p_{10} = 1.259 \cdot 10^{-3}$, $p_{01} = 0.4377$, $p_{20} = -7.513 \cdot 10^{-7}$, $p_{11} = 1.284 \cdot 10^{-3}$, $p_{02} = -10.13$, and root mean square residual equal to

Table 4: Predicted and measured performance data for different DJI F550 configurations equipped with the same battery pack (Li–Po, $N_s = 4$, $C_0 = 9$ Ah, $K = 0.6$).

Configuration	W_0 [N]	Propeller	f	η_e	P_b est. [W]	P_b meas. [W]	ε_P [%]	t_f est. [min]	t_f meas. [min]	ε_t [%]
MR6-9	18.51	1	0.683	0.646	468.2	459.3	1.94	10.03	9.83	2.03
MR7-9	13.24	1	0.676	0.625	351.4	352.3	-0.26	13.45	13.05	3.07
MR8-9	18.86	4	0.668	0.584	432.2	426.0	1.46	10.88	10.77	1.02
MR9-9	13.59	4	0.654	0.557	334.5	342.2	-2.26	14.15	14.13	0.14

0.015.

Starting from the reference platform described above, 4 different multi-rotor configurations are defined, which differ by the selection of propellers (the ones marked as 1 and 4 in Table 1) and the particular empty–operative weight W_0 (varied by the quantity $\Delta W_0|_{pl} = 5.27$ N through the equipment of an additional 0.537 kg payload system). For each configuration, a flight test was performed at temperature $\tau = 26$ °C and pressure $p = 97\,903$ Pa (estimated air density $\rho = 1.1401$ kg/m^3 and dynamic viscosity $\mu = 1.841 \cdot 10^{-5}$ Pa s) while discharging the battery to the 60% of nominal capacity ($C_f = K\,C_0 = 0.6 \cdot 9 = 5.4$ Ah). Main results are reported in Table 4 in terms of model–predicted figure of merit, electrical efficiency, battery power, and flight endurance. To this end, battery coefficients, evaluated from Eqs. (21)–(25), are $\delta = 17.93$, $\epsilon = -1.025$, and $\beta = 0.9632$. Data are compared to measured values and estimation errors are calculated. Note that, in the same loading condition, the adoption of Propellers '4' determines a total increase of empty weight by about $\Delta W_0|_{prop} = 0.35$ N with respect to the case in which propellers '1' are adopted. It is evident from Table 4 that, for all the analyzed configurations, the estimation errors of both battery power (ε_P) and flight time (ε_t) are lower than 5%, which vindicates the validity of the proposed approach.

In Figure 10 the discussion of the sizing procedure illustrated in Section 4.2 is applied to the present case, while comprising the data points already reported in Table 4 (round markers). In particular, the curves representing predicted endurance are plotted as a function of nominal capacity for all the considered configurations. The presence of a maximum in all the

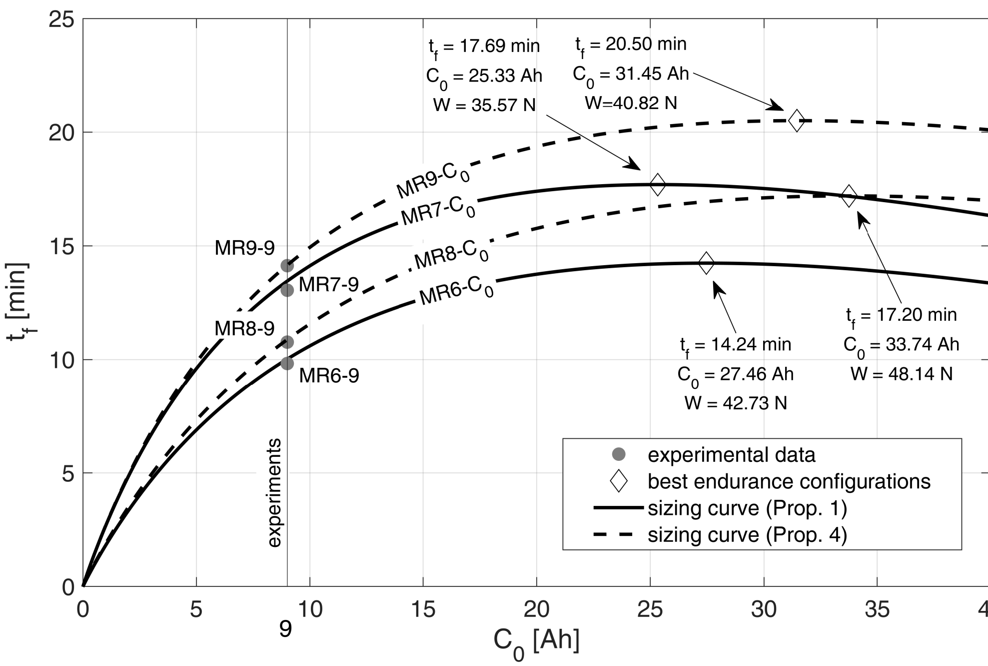

Figure 10: Predicted and measured performance data for different DJI F550 configurations (the symbol 'MRX-Y' refers to multirotor configuration 'X' with battery nominal capacity 'Y' Ah).

curves clearly points out that, if endurance is pursued as the most relevant goal in the design process, it is useless to increase the size of the battery pack beyond a certain limit, provided that the corresponding growth in rotorcraft weight affects required power. Best endurance configurations are indicated in Fig. 10 by diamond markers. Note that, for all the considered configurations, the maximum is 'flat', meaning that very large variations of battery weight are necessary for marginal gains in terms of expected flight time. From the practical standpoint, this growth in battery capacity is clearly not justified, when one considers that a bigger battery is more expensive and the corresponding additional weight typically requires more powerful motors and robust structures.

As an example, consider configuration $MR6-9$ in Fig. 10, for which the predicted hover endurance is 10.03 min when $K = 0.6$. Assume that, in order to comply with more stringent requirements, the endurance must be extended by 2 minutes with the same discharge percentage. Taking into account Figure 10, the target flight time of 12.03 min can be obtained in 2 ways. In the first case, the same set of propellers is used (Propellers 1) but a bigger battery with nominal capacity equal to at least 13.09 Ah is required (corresponding take–off weight: $W = 30.75$ N). In the second case, the multirotor is equipped with Propellers 4 and a bigger battery with at least 10.72 Ah (take–off weight: $W = 28.32$ N). At the time of writing the present paper, the considered battery type by Tattu is characterized by a cost of about 15.60 US dollars per Ah [65]. The complete sets of Propellers 1 and 4, equivalent to the DJI product, respectively cost 4.50 and 7.50 dollars, according to [56]. With this in mind, the first upgrade solution would determine an additional cost of $4.09 \cdot 15.60 = 63.80$ dollars (battery upgrade). The second solution would require 29.83 dollars, of which $1.72 \cdot 15.60 = 26.83$ dollars for the battery upgrade and only 3 dollars for the replacement of the full propellers set.

The model derived in Eqs. (34)–(38), which analytically provides an approximate value to the best endurance capacity, is finally validated. The exact best endurance configurations are detailed in Figure 10. The minimum estimation error is obtained for platform $MR9 - C_0$, where $W_{be} = 40.82$ N and $W^{\star}_{be} = 41.96$ N, and is equal to +2.79%. The maximum error is obtained for platform $MR8 - C_0$, where $W_{be} = 48.14$ N and $W^{\star}_{be} = 54.36$ N, and is equal to +12.92%.

6. Conclusions

Performance of an electrically–powered multirotor is discussed by means of a novel integral formulation for constant–power battery–discharge process. The analysis is based on the estimation of power required from the battery pack during a hovering condition. Starting from the results available from blade element theory, an analytical expression is derived, on an experimental basis, for the figure of merit of a class of commercial–off–the–shelf propellers. The main outcome from these propeller tests is discussed, provided that the blade Reynolds number plays a significant part in determining its performance. As a by–product, the trim angular rate of the rotors and the torque applied by the electric motors to the propellers are derived.

Numerical simulations and an experimental campaign validate the capability of the proposed approach to accurately predict the hover endurance of existing platforms. At the same time, a very simple procedure is outlined to design novel configurations or upgrade a selected propulsion system, in order to satisfy given requirements in terms of flight time, take–off weight, and prototyping costs. In this respect, a closed–form solution to the best endurance battery capacity is also derived. The effectiveness of the proposed approach and the simplicity of the analytical formulation are shown to be of general validity and prove to be encouraging in the framework of rotorcraft preliminary sizing.

Future developments, allowing for improved performance prediction and optimal sizing procedures include: 1) detailed characterization of the induced flow by the propeller in order to further investigate the contribution of both induced and profile power; 2) the extension of the applicability field of the proposed method to a wider family of commercial–of–the–shelf propellers, including counter–rotating configurations, thus relaxing the requirements of Assumption 1; 3) the derivation of estimation algorithms to perform battery parameter identification in–flight; 4) the adaptation of the proposed method to the analysis of different flight conditions, such as cruise, climb, or descent, with the aim to accurately estimate the required power, endurance, and range performance, and to provide sizing guidelines for complex mission scenarios.

References

[1] S. Harwey, A. Lucieer, Assessing the Accuracy of Georeferenced Point Clouds Produced via Multi–View Stereopsis from Unmanned Aerial Vehicle (UAV) Imagery, J. Remote Sensing, Vol. 4, No. 6, 2012, 1573–1599, doi: 10.3390/rs4061573

[2] G. Cai, J. Dias, L. Seneviratne, A Survey of Small–Scale Unmanned Aerial Vehicles: Recent Advances and Future Development Trends, Unmanned Systems, Vol. 2, No. 2, 2014, 175–199, doi: 10.1142/S2301385014300017

[3] E.L. de Angelis, F. Giulietti, G. Rossetti, Multirotor aircraft formation

flight control with collision avoidance capability, Aerosp. Sci. Technol., Vol. 77, June 2018, 733–741, doi: 10.1016/j.ast.2018.04.002

[4] K. Valavanis, G.J. Vachtsevanos, Handbook of Unmanned Aerial Vehicles, Springer Reference Vol. 1, Netherlands, 2015, 308–309.

[5] E.L. de Angelis, et al., Optimal autonomous multirotor motion planning in an obstructed environment, Aerosp. Sci. Technol., Vol. 87, April 2019, 379–388, doi: 10.1016/j.ast.2019.03.017

[6] E.L. de Angelis, Stability analysis of a multirotor vehicle hovering condition, Aerosp. Sci. Technol., Vol. 72, Jan. 2018, 248–255, doi: 10.1016/j.ast.2017.11.017

[7] Z. Zhang, J. Li, J. Wang, J., Sequential convex programming for nonlinear optimal control problems in UAV path planning, Aerosp. Sci. Technol., Vol. 76, May 2018, 280–290, doi: 10.1016/j.ast.2018.01.040

[8] M.H. Hwang, H.R. Cha, S.Y. Jung, Practical Endurance Estimation for Minimizing Energy Consumption of Multirotor Unmanned Aerial Vehicles, Energies, Vol. 11, No. 9, Aug. 2018, 1–11, doi: 10.3390/en11092221

[9] Z. Xunfei, et al., Cycle life estimation of lithium–ion polymer batteries using artificial neural network and support vector machine with time–resolved thermography, Microelectron. Reliab., Vol. 79, 2017, 48–58, doi: 10.1016/j.microrel.2017.10.013

[10] X. Hu, D. Cao, B. Egardt, Condition monitoring in advanced battery management systems: moving horizon estimation using a reduced elec-

trochemical model, IEEE ASME Trans. Mechatron., Vol. 23, No. 1, 2017, 167–178, doi: 10.1109/TMECH.2017.2675920

[11] Q. Zhang, et al., Electrochemical model of lithium-ion battery for wide frequency range applications, Electrochim. Acta, Vol. 343, 2020, doi: 10.1016/j.electacta.2020.136094

[12] S. Nejad, D.T. Gladwin, D.A. Stone, A systematic review of lumped-parameter equivalent circuit models for real-time estimation of lithium-ion battery states, J. Power Sources, Vol. 316, 2016, 183–196, doi: 10.1016/j.jpowsour.2016.03.042

[13] Y. Wang, et al., Probability based remaining capacity estimation using data-driven and neural network model, J. Power Sources, Vol. 315, 2016, 199–208, doi: 10.1016/j.jpowsour.2016.03.054

[14] E.L. de Angelis, et al., Terminal height estimation using a Fading Gaussian Deterministic filter, Aerosp. Sci. Technol., Vol. 55, 2016, 366–376, doi: 10.1016/j.ast.2016.06.013

[15] Y. Wang, et al., A comprehensive review of battery modeling and state estimation approaches for advanced battery management systems, Renewable and Sustainable Energy Reviews, Vol. 131, 2020, 1–18, doi: 10.1016/j.rser.2020.110015

[16] W. Peukert, Über die Abhängigkeit der Kapazität von der Entladestromstärke bei Bleiakkumulatoren, Elektrotechnische Zeitschrift, Vol. 20, 1897, 20–21.

[17] L.W. Traub, Range and Endurance Estimates for Battery–Powered Aircraft, J. Aircraft, Vol. 48, No. 2, March 2011, 703–707, doi: 10.2514/1.C031027

[18] G. Avanzini, F. Giulietti, F., Maximum Range for Battery–Powered Aircraft, J. Aircraft, Vol. 50, No. 1, Jan. 2013, pp. 304-307; doi: 10.2514/1.C031748

[19] L.W. Traub, Validation of endurance estimates for battery powered UAVs, Aeronautical Journal, Vol. 117, No. 1197, 2013, 1155–1166, doi: 10.1017/S0001924000008757

[20] M. Gatti, F. Giulietti, M. Turci, Maximum Endurance for Battery–Powered Rotary-Wing Aircraft, Aerosp. Sci. Technol., Vol. 45, 2015, 174–179, doi: 10.1016/j.ast.2015.05.009

[21] P. Lindahl, I. Moog, S.R. Shaw, Simulation, design, and validation of an UAV SOFC propulsion System, IEEE Trans. Aerosp. Electron. Syst., Vol. 48, No. 3, 2012, 2582–2591, doi: 10.1109/TAES.2012.6237610

[22] E.S. Latorre, Propulsion system optimization for an unmanned light weight quadrotor (dissertation), Universitat Politecnica de Catalunya, Barcelona, 2011.

[23] D. Kaya, et al., Propulsion system selection and modeling for a quadrotor with search and rescue mission, 54th AIAA Aerospace Sciences Meeting, Jan. 4-8, 2016, Reston, California, 1–10, 10.2514/6.2016-1528

[24] A. Abdilla, A. Richards, S. Burrow, Power and endurance modelling of battery-powered rotorcraft, 2015 IEEE/RSJ International Conference

on Intelligent Robots and Systems (IROS), Sept. 28–Oct. 2, 2015, Hamburg, Germany, 675–680, doi: 10.1109/IROS.2015.7353445

[25] A. Abdilla, A. Richards, S. Burrow, Endurance optimization of battery-powered rotorcraft, Towards Autonomous Robotic systems, 16th Annual Conference, Sept 8–10, 2015, Liverpool, England, 1–12, doi: 10.1007/978-3-319-22416-9

[26] M.E. Fuller, A Battery Model for Constant–Power Discharge Including Rate Effects, Energy Conversion and Management, Vol. 88, 2014, 199–205, doi: 10.1016/j.enconman.2014.08.015

[27] G. Avanzini, E.L. de Angelis, F. Giulietti, Optimal performance and sizing of a battery–powered aircraft, Aerosp. Sci. Technol., Vol. 59, 2016, 132–144, doi: 10.1016/j.ast.2016.10.015

[28] M. Cerny, C. Breitsamter, Investigation of small–scale propellers under non–axial inflow conditions, Aerosp. Sci. Technol., Vol. 106, Nov. 2020, 1–14, doi: 10.1016/j.ast.2020.106048

[29] G. Gupta, S. Abdallah, Propeller Force–Constant Modeling for Multirotor UAVs from Experimental Estimation of Inflow Velocity, International J. Aerospace Engineering, Vol. 2018, 2018, 1–10, doi: 10.1155/2018/9632942

[30] S. Delbecq, et al., Efficient sizing and optimization of multirotor drones based on scaling laws and similarity models, Aerosp. Sci. Tecnol., Vol. 102, July 2020, 1–23, doi: 10.1016/j.ast.2020.105873

[31] D. Shukla, N. Komerath, Multirotor Drone Aerodynamic Interaction Investigation, Drones, Vol. 2, No. 43, 2018, 1–13, doi: 10.3390/drones2040043

[32] N.A. Vu, D.K. Dang, T. Le Dinh, Electric propulsion system sizing methodology for an agriculture multicopter, Aerosp. Sci. Technol., Vol. 90, 2019, 314–326, doi: 10.1016/j.ast.2019.04.044

[33] H. Zhu, et al., Design and assessment of octocopter drones with improved aerodynamic efficiency and performance, Aerosp. Sci. Technol., Vol. 106, Nov. 2020, 1–16, doi: 10.1016/j.ast.2020.106206

[34] D.M. Filatov, A.V. Devyatkin, A.I. Friedrich, Quadrotor parameters identification and control system design, 2017 IEEE Conference of Russian Young Researchers in Electrical and Electronic Engineering (EIConRus), Feb. 1–3, St. Petersburg, Russia, 2017, 826–830, doi: 10.1109/EIConRus.2017.7910684

[35] C.E. Tinney, J. Sirohi, Multirotor Drone Noise at Static Thrust, AIAA Journal, Vol. 56, No. 7, July 2018, 2816–2826, doi: 10.2514/1.J056827

[36] Z.J. Chen, A. Stol, P.J. Richards, Preliminary design of multirotor UAVs with tilted–rotors for improved disturbance rejection capability, Aerosp. Sci. Technol., Vol. 92, 2019, 635–643, doi: 10.1016/j.ast.2019.06.038

[37] E.V. Loureiro, et al., Evaluation of low fidelity and CFD methods for the aerodynamic performance of a small propeller, Aerosp. Sci. Technol., Vol. 108, Jan. 2021, 1–17, doi: 10.1016/j.ast.2020.106402

[38] B.W. McCormick, Aerodynamics, Aeronautics, and Flight Mechanics, 2nd Edition, John Wiley & Sons, Inc., New York, 1994, 413–419.

[39] J.G. Leishman, Principles of Helicopter Aerodynamics, 2nd Edition, Cambridge University Press, New York, 2006, Chs. 2 and 5.

[40] R.W. Deters, G.K. Ananda, M.S. Selig, Reynolds Number Effects on the Performance of Small–Scale Propellers, 32nd AIAA Applied Aerodynamics Conference, June 16–20, Atlanta, GA, 2014, 1–43, doi: 10.2514/6.2014-2151

[41] M. Wang, et al., Battery package design optimization for small electric aircraft, Chinese Journal of Aeronautics, Vol. 33, No. 11, 2020, 2864–2876, doi: 10.1016/j.cja.2020.04.021

[42] Z. Ma, et al., Convex modeling for optimal battery sizing and control of an electric variable transmission powertrain, Oil & Gas Science and Technology, Vol. 74, No. 25, 2019, 1–13, doi: 10.2516/ogst/2018104

[43] X.Z. Gao, et al., Joint optimization of battery mass and flight trajectory for high-altitude solar-powered aircraft, Proc. of the Institution of Mechanical Engineers, Part G, Vol. 228, No. 13, 2014, 2439–2451, doi: 10.1177/0954410013518510

[44] W. Johnson, Helicopter Theory, Dover Publications, Inc., New York, 1994, 299–300.

[45] A. Gong, R. MacNeill, D. Verstraete, Performance Testing and Modeling of a Brushless DC Motor, Electronic Speed Controller and Propeller for

a Small UAV, AIAA 2018–4584, 2018 Joint Propulsion Conference, July 9–11, Cincinnati, Ohio, 2018, 1–15, doi: 10.2514/6.2018-4584

[46] A.M. Harrington, C. Kroninger, Characterization of Small DC Brushed and Brushless Motors, USA Army Research Laboratory Tech. Report ARL–TR–6389, 2013, 1–48

[47] Solutions for All Markus Müller, eCalc - The most reliable RC Calculator on the Web, Retrieved from https://www.ecalc.ch, 2021.

[48] C. Persson, Drive Calculator, Retrieved from http://www.drivecalc.de, 2021.

[49] C.N. Keys, Rotary-Wing Aerodynamics - Volume II - Performance Prediction of Helicopters, NASA Contractor Report 3083, Jan. 1979, Ch. 2.

[50] I.H. Abbott, A.E. Von Doenhoff, Theory of wing sections, Dover Publications, Inc., New York, 1959, Ch. 5.

[51] S.F. Hoerner, Fluid Dynamic Drag: Practical Information on Aerodynamic Drag and Hydrodynamic Resistance, Hoerner Fluid Dynamics, Published by the Author, Bakersfield, CA, 1965, Ch. 2.

[52] D. Sartori, W. Yu, Experimental Characterization of a Propulsion System for Multi–rotor UAVs, J. Intell. Robot. Syst., Vol. 96, 2019, 529–540, doi: 10.1007/s10846-019-00995-2

[53] DJI, Professional, Enterprise, and Agriculture Drones, Retrieved from https://www.dji.com, 2021.

[54] FreeFly Systems, Professional Drones, Retrieved from https://www.freeflysystems.com, 2021.

[55] Yuneec, Yuneec Drones for Commercial Use, Retrieved from https://www.yuneec.com, 2021.

[56] RC Timer, Commercial/Industrial Propellers, Retrieved from https://www.rctimer.com/commercial-industrial-propellers-c0420, 2021.

[57] T–Motor, Carbon Fiber and Polymer Propellers, Retrieved from https://store-en.tmotor.com/category.php?id=4, 2021.

[58] W.H. Press, et al., Numerical recipes: the art of scientific computing - 2nd Edition, Cambridge University Press (1992), Chs. 5, 9, and 10.

[59] R.P. Brent, Algorithms for minimization without derivatives, Prentice–Hall (2013), Ch. 5.

[60] D. Curtiss, Recent extensions of Descartes' rule of signs, Annals of Maths Vol. 19, No. 4, 1918, 251–278.

[61] M. Gatti, Complete Preliminary Design Methodology for Electric Multirotor, J. Aerosp. Eng., Vol. 30, Issue 5, 2017, 1–15, doi: 10.1061/(ASCE)AS.1943-5525.0000752

[62] DJI, E2000–Tuned Propulsion System, Retrieved from https://www.dji.com/en/e2000, 2021.

[63] M. Biczyski, et al., Multirotor Sizing Methodology with Flight Time Estimation, J. Advanced Transportation, Vol. 2020, 2020, 1–15, doi: 10.1155/2020/9689604

[64] T–Motor, U8 KV135 Efficiency Type, Retrieved from https://store-en.tmotor.com/goods.php?id=323, 2021.

[65] Tattu Batteries, Retrieved from https://www.genstattu.com, 2021.